Central-Upwind Scheme for a Non-hydrostatic Saint-Venant System

Alina Chertock*, Alexander Kurganov†, Jason Miller‡ and Jun Yan§

Abstract

We develop a second-order central-upwind scheme for the non-hydrostatic version of the Saint-Venant system recently proposed in [M.-O. Bristeau and J. Sainte-Marie, *Discrete Contin. Dyn. Syst. Ser. B,* 10 (2008), pp. 733–759]. The designed scheme is both well-balanced (capable of exactly preserving the "lake-at-rest" steady state) and positivity preserving. We then use the central-upwind scheme to study ability of the non-hydrostatic Saint-Venant system to model long-time propagation and on-shore arrival of the tsunami-type waves. We discover that for a certain range of the dispersive coefficients, both the shape and amplitude of the waves are preserved even when the computational grid is relatively coarse. We also demonstrate the importance of the dispersive terms in the description of on-shore arrival.

Key words: hyperbolic systems of balance laws, dispersive shallow water systems, Godunov-type central-upwind schemes.

1 Introduction

Tsunami waves are characterized by having a relatively low amplitude, large wavelength, and large characteristic wave speed, see, e.g., [7, 27, 31]. In fact, the amplitude of a tsunami wave can be so small that it may not even be noticed by a ship traveling through it in deep water. Because of their speed and wavelength, however, these waves contain a tremendous amount of energy. When the depth of the water decreases (in the beginning of the on-shore arrival stage of tsunami wave propagation), tsunamis undergo a process called wave shoaling, in which the wave slows down and the wavelength decreases. In order to conserve energy, it is transformed from kinetic to potential energy and the wave amplitude increases. This potential energy can then be released in disastrous fashion when the wave comes to shore. It is therefore very important to have accurate models and corresponding numerical methods for tsunami waves in order to mitigate any catastrophe that may result.

*Department of Mathematics, North Carolina State University, Raleigh, NC 27695, USA; chertock@math.ncsu.edu

†Department of Mathematics, Southern University of Science and Technology, Shenzhen, 518055, China and Mathematics Department, Tulane University, New Orleans, LA 70118, USA; kurganov@math.tulane.edu

‡Applied Physics Laboratory, Johns Hopkins University, Laurel, MD 20723, USA; seeyouken@gmail.com

§Department of Mathematics, North Carolina State University, Raleigh, NC 27695, USA; jyan9@ncsu.edu

One model used for shallow water waves is the classical Saint-Venant system [12], which is a depth-averaged system that can be derived from the Navier-Stokes equations (see, e.g., [14]). The Saint-Venant system is a very good simplification for lakes, rivers, and coastal areas in which the typical time and space scales of interest are relatively short. Tsunami waves form in deep water and travel very long distances (thousands of kilometers) before coming to the shore. Over long time, solutions of the Saint-Venant system break down, dissipate in an unphysical manner, shock waves develop, and the system fails to capture small, trailing waves that are seen in nature and laboratory experiments [29]. Thus, it is necessary to use a more sophisticated model in order to preserve the wave characteristics over long time simulations.

Non-hydrostatic models (the celebrated Green-Naghdi equation [17] and several others, see, e.g., [1, 3, 4] and references therein) work well for long-time propagation of tsunami-like waves because they allow the wave to travel for long distances without decaying in amplitude. In addition, since these systems are dispersive, they give rise to trailing waves that are observed to follow tsunamis in nature. However, it is necessary to achieve some balance between dispersion observed with a non-hydrostatic model and the dissipation seen in the classical Saint-Venant system.

The non-hydrostatic Saint-Venant system presented in [5, 6] is given by

$$\begin{cases} h_t + (hu)_x = 0, \\ (hu)_t + M_t + \left(hu^2 + \dfrac{g}{2}h^2\right)_x + N = -ghB_x + p^a w_x - 4(\nu u_x)_x - \kappa(h, hu)u, \end{cases} \tag{1.1}$$

where $h(x,t)$ is the water depth measured vertically from the bottom topography, described by function $B(x,t)$, $u(x,t)$ is the vertically averaged velocity, hu is the horizontal momentum or discharge, $p^a = p^a(x,t)$ is the atmospheric pressure function, $w := h + B$ is the free surface, ν is the viscosity coefficient, κ is the friction function, and M and N are defined as

$$M(h, hu, B) = \left(-\frac{1}{3}h^3 u_x + \frac{1}{2}h^2 B_x u\right)_x + B_x\left(-\frac{1}{2}h^2 u_x + B_x hu\right),$$

and

$$N(h, hu, B) = \left((h^2)_t(hu_x - B_x u)\right)_x + 2B_x h_t(hu_x - B_x u) - B_{xt}\left(-\frac{1}{2}h^2 u_x + B_x hu\right). \tag{1.2}$$

Here, M and N are terms that arise when the system is derived from the Euler equations and include non-hydrostatic pressure terms [6].

One of the goals of the current work is to numerically study the effects of the dispersion terms present in the non-hydrostatic model (1.1). To this end, we introduce the *new scaling parameters* α_M and α_N as coefficients to M and N in (1.1). For the purpose of this work we will neglect fluid viscosity and friction by setting ν and $\kappa(h, hu)$ to be identically zero and also assume that the bottom topography function is independent of time, i.e., $B = B(x)$. In addition, we follow the approach in [20, 24] and rewrite our system in terms of the equilibrium variables $w = h + B$ and $q := hu$:

$$\begin{cases} w_t + q_x = 0, \\ q_t + \alpha_M M_t + \left(\dfrac{q^2}{w - B} + \dfrac{g}{2}(w - B)^2\right)_x + \alpha_N N = -g(w - B)B_x + p^a w_x. \end{cases} \tag{1.3}$$

When $\alpha_M = \alpha_N = p^a \equiv 0$, (1.3) reduces to the classical Saint-Venant system, and as we increase these parameters, the amount of dispersion in our model increases and the effects of the lack of the hydrostatic pressure assumption should be apparent.

To study the non-hydrostatic effects, we design a highly accurate and robust numerical method for (1.3). A good scheme for this model should be well-balanced (it should exactly preserve "lake-at-rest" steady-state solutions at the discrete level), it should preserve positivity of h, and it should be able to properly handle discontinuous/nonsmooth solutions. The system (1.3) presents challenges in the approximation and treatment of the higher-order mixed derivatives in the non-hydrostatic terms whose semi-discretization leads to stiff terms that require an efficient numerical solver for the resulting system of ODEs. In this paper, we develop a central-upwind scheme for (1.3) which possesses all of the aforementioned features and use it to examine the effects of the non-hydrostatic pressure terms on the propagation of waves over long times and on their on-shore arrival.

Central-upwind schemes (first introduced in [26] and further developed in [21,23]) are Godunov-type finite volume methods. They belong to the class of Riemann-problem-solver-free central schemes and thus can be applied to a variety of hyperbolic systems of conservation laws as a "black-box" solver. When central-upwind schemes are applied to systems of balance laws, a special treatment of the source terms appearing in the system at hand must be developed. This was done for single- and two-layer shallow water models in [2,9–11,19,20,24,25]. In order to apply the central-upwind scheme to (1.3), one needs to specify the way the terms on the right-hand side (RHS) of (1.3) are discretized. As it was mentioned above, this should be done in such a way that physically relevant steady-state solutions are exactly preserved and h is *guaranteed* to be nonnegative.

The physically relevant steady-state solution for (1.3) is the "lake-at-rest" solution, corresponding to the water surface being perfectly flat and stationary:

$$w = h + B \equiv \text{Const}, \qquad hu \equiv 0. \tag{1.4}$$

Preserving this particular steady state would guarantee that no artificial surface waves are generated, and also ensure that small perturbations of the water surface will not lead to a "numerical storm". This is achieved by using a special discretization of the geometric source term on the RHS of (1.3) which is presented in Section 2.1.3.

Preserving positivity of h is essential since solutions containing negative h would not only be unphysical, but will cause the numerical computations to fail. To ensure positivity of h, we follow the idea from [24]. We first replace the bottom topography with its continuous piecewise linear approximation and then adjust the piecewise linear reconstruction of the water heights, ensuring that through each computational cell the depth of each layer is nonnegative. This is presented in Section 2.1.1.

With the numerical method in place, we examine the effect of the non-hydrostatic pressure terms in Section 3, where we try to strike a balance between dissipation and dispersion inherent in the system.

2 Numerical Method

2.1 Central-Upwind Scheme

We develop a new well-balanced positivity preserving scheme for (1.3), which is based on the semi-discrete central-upwind scheme from [23] (see also [24,25]). For simplicity, we introduce a uniform grid $x_j = j\Delta x$ where Δx is a small spatial scale, and denote the computational cells centered at x_j by $I_j := [x_{j-\frac12}, x_{j+\frac12}]$.

We rewrite the system (1.3) in the following form:

$$\mathbf{U}_t + \mathcal{M}(\mathbf{U},B)_t + \mathbf{F}(\mathbf{U},B)_x + \mathcal{N}(\mathbf{U},B) = \mathbf{S}(\mathbf{U},B), \quad \mathbf{U} := (w,q)^\top \tag{2.1}$$

where

$$\mathbf{F}(\mathbf{U},B) = \Big(q, \frac{q^2}{w-B} + \frac{g}{2}(w-B)^2\Big)^T, \quad \mathbf{S}(\mathbf{U},B) = (0, -g(w-B)B_x + p^a w_x)^\top,$$
$$\mathcal{M}(\mathbf{U},B) = (0, \alpha_M M(\mathbf{U},B))^T, \quad \mathcal{N}(\mathbf{U},B) = (0, \alpha_N N(\mathbf{U},B))^T.$$

Using the above notations, a semi-discrete central-upwind scheme for (2.1) takes the form of the following system of time-dependent ODEs:

$$\frac{d}{dt}\big(\overline{\mathbf{U}}_j(t) + \overline{\mathcal{M}}_j(t)\big) = -\frac{\mathbf{H}_{j+\frac12}(t) - \mathbf{H}_{j-\frac12}(t)}{\Delta x} + \overline{\mathbf{S}}_j(t) - \overline{\mathcal{N}}_j(t), \tag{2.2}$$

where $\overline{(\cdot)}_j(t)$ is used to denote the approximated cell averages over the corresponding cells:

$$\overline{\mathbf{U}}_j(t) \approx \frac{1}{\Delta x}\int\limits_{I_j} \mathbf{U}(x,t)\,dx, \qquad \overline{\mathbf{S}}_j(t) \approx \frac{1}{\Delta x}\int\limits_{I_j} \mathbf{S}(\mathbf{U}(x,t),B(x))\,dx,$$
$$\overline{M}_j(t) \approx \frac{1}{\Delta x}\int\limits_{I_j} M(\mathbf{U}(x,t),B(x))\,dx, \qquad \overline{N}_j(t) \approx \frac{1}{\Delta x}\int\limits_{I_j} N(\mathbf{U}(x,t),B(x))\,dx,$$

and $\mathbf{H}_{j+\frac12}(t)$ are the central-upwind numerical fluxes $\mathbf{H}_{j+\frac12}$ proposed in [24] (see also [21,23]):

$$\mathbf{H}_{j+\frac12}(t) = \frac{a^+_{j+\frac12}\mathbf{F}\left(\mathbf{U}^-_{j+\frac12}, B_{j+\frac12}\right) - a^-_{j+\frac12}\mathbf{F}\left(\mathbf{U}^+_{j+\frac12}, B_{j+\frac12}\right)}{a^+_{j+\frac12} - a^-_{j+\frac12}} + \frac{a^+_{j+\frac12}a^-_{j+\frac12}}{a^+_{j+\frac12} - a^-_{j+\frac12}}\left[\mathbf{U}^+_{j+\frac12} - \mathbf{U}^-_{j+\frac12}\right]. \tag{2.3}$$

Here, the values $\mathbf{U}^\pm_{j+\frac12}$ are the right/left point values at $x = x_{j+\frac12}$ of the conservative piecewise linear reconstruction $\widetilde{\mathbf{U}}$,

$$\widetilde{\mathbf{U}}(x) := \overline{\mathbf{U}}_j + (\mathbf{U}_x)_j\,(x - x_j)\,, \quad x_{j-\frac12} < x < x_{j+\frac12}, \tag{2.4}$$

which is used to approximate $\mathbf{U}$ at time t, that is,

$$\mathbf{U}^\pm_{j+\frac12} := \widetilde{\mathbf{U}}\left(x_{j+\frac12} \pm 0\right) = \overline{\mathbf{U}}_{j+\frac12\pm\frac12} \mp \frac{\Delta x}{2}\,(\mathbf{U}_x)_{j+\frac12\pm\frac12}\,. \tag{2.5}$$

The numerical derivatives $(\mathbf{U}_x)_j$ are at least first-order accurate component-wise approximations of $\mathbf{U}_x(x_j,t)$, computed using a nonlinear limiter needed to ensure the non-oscillatory nature of the reconstruction (2.4). The right- and left-sided local speeds $a^{\pm}_{j+\frac{1}{2}}$ in (2.3) are obtained from the smallest and largest eigenvalues of the Jacobian $\frac{\partial \mathbf{F}}{\partial \mathbf{U}}$ (see Section 2.1.1 for details). Notice that the terms $\mathbf{U}^{\pm}_{j+\frac{1}{2}}$, $\overline{\mathbf{U}}_j$, $a^{\pm}_{j+\frac{1}{2}}$, $\widetilde{\mathbf{U}}(x)$ and $(\mathbf{U}_x)_j$ all depend on t, but we suppress this dependence for simplicity.

We also follow the work of [24,25] and replace $B(x)$ in (2.3) with its continuous piecewise linear approximation by defining

$$B_{j+\frac{1}{2}} := B(x_{j+\frac{1}{2}}) \quad \text{and} \quad B_j := \frac{1}{2}(B_{j+\frac{1}{2}} + B_{j-\frac{1}{2}}). \tag{2.6}$$

This will help to ensure the positivity preserving nature of the proposed scheme, as we show below.

2.1.1 Positivity-Preserving Reconstruction

The use of a piecewise linear reconstruction (2.4) requires the computation of slopes $(\mathbf{U}_x)_j$ to obtain the right/left point values defined in (2.5). It is well-known that in order to ensure the non-oscillatory nature of the reconstruction, the use of a nonlinear limiter is required. We choose to use the generalized minmod limiter:

$$(\mathbf{U}_x)_j = \text{minmod}\left(\theta\frac{\overline{\mathbf{U}}_j - \overline{\mathbf{U}}_{j-1}}{\Delta x}, \frac{\overline{\mathbf{U}}_{j+1} - \overline{\mathbf{U}}_{j-1}}{2\Delta x}, \theta\frac{\overline{\mathbf{U}}_{j+1} - \overline{\mathbf{U}}_j}{\Delta x}\right), \quad \theta \in [1,2], \tag{2.7}$$

where the minmod function defined as

$$\text{minmod}(z_1, z_2, \dots) := \begin{cases} \min\limits_j\{z_j\}, & \text{if } \ z_j > 0 \ \forall j, \\ \max\limits_j\{z_j\}, & \text{if } \ z_j < 0 \ \forall j, \\ 0, & \text{otherwise,} \end{cases}$$

is applied in a componentwise manner. The parameter θ can be used the control the amount of numerical viscosity present in the resulting scheme (see, e.g., [28,30,33] for more details concerning the generalized minmod and other nonlinear limiters).

Even when all of the cell averages $\overline{h}_j$ are nonnegative, the reconstructed right/left point values at the cell interface $h^{\pm}_{j+\frac{1}{2}}$ may be negative. To guarantee positivity of h throughout the entire computational domain, we follow the procedure from [24] and amend the reconstruction (2.4), (2.5), (2.7) in the following conservative way:

$$\begin{aligned} &\text{if } w^-_{j+\frac{1}{2}} < B_{j+\frac{1}{2}}, \ \text{ then take } (w_x)_j := -\frac{\overline{w}_j}{\Delta x/2} \implies w^-_{j+\frac{1}{2}} = B_{j+\frac{1}{2}}, \quad w^+_{j-\frac{1}{2}} = 2\overline{w}_j, \\ &\text{if } w^+_{j-\frac{1}{2}} < B_{j-\frac{1}{2}}, \ \text{ then take } (w_x)_j := \frac{\overline{w}_j}{\Delta x/2} \implies w^-_{j+\frac{1}{2}} = 2\overline{w}_j, \quad w^+_{j-\frac{1}{2}} = B_{j-\frac{1}{2}}. \end{aligned} \tag{2.8}$$

It is necessary to compute the nonconservative quantity $u = q/h$ for the computation of numerical fluxes and local propagation speeds. We follow the desingularization procedure outlined in [24,25] to avoid possible division by small values of h:

$$u := \frac{\sqrt{2}(w-B)\cdot q}{\sqrt{(w-B)^4 + \max\left((w-B)^4, \varepsilon\right)}}, \tag{2.9}$$

where ε is a small desingularization parameter (in our numerical experiments, we have taken $\varepsilon = \min((\Delta x)^3, 10^{-4})$). Notice that this procedure will only affect the velocity computations when $h^4 < \varepsilon$. It is also important to recalculate the values of q at the points where the velocity was desingularized by setting

$$q := h \cdot u.$$

Since the flux term $\mathbf{F}$ in (2.1) is equivalent to that of the classical Saint-Venant system, the local propagation speeds $a^{\pm}_{j+\frac{1}{2}}$ are computed the same way using the eigenvalues of $\frac{\partial \mathbf{F}}{\partial \mathbf{U}}$:

$$\begin{aligned} a^{+}_{j+\frac{1}{2}} &:= \max\left\{u^{+}_{j+\frac{1}{2}} + \sqrt{gh^{+}_{j+\frac{1}{2}}},\, u^{-}_{j+\frac{1}{2}} + \sqrt{gh^{-}_{j+\frac{1}{2}}},\, 0\right\},\\ a^{-}_{j+\frac{1}{2}} &:= \min\left\{u^{+}_{j+\frac{1}{2}} - \sqrt{gh^{+}_{j+\frac{1}{2}}},\, u^{-}_{j+\frac{1}{2}} - \sqrt{gh^{-}_{j+\frac{1}{2}}},\, 0\right\}. \end{aligned}$$

Remark 2.1 Proof of the positivity preserving property of this reconstruction is available in [20, 24].

2.1.2 Discretization of the Non-hydrostatic Pressure Terms

The dispersive terms $\overline{M}_j$ and $\overline{N}_j$ are computed using the second-order midpoint rule. We first follow [5] and discretize the terms of M at x_j in the following ways:

$$\begin{aligned} \left(\frac{1}{3}h^3u_x\right)_x(x_j) &\approx \frac{1}{3\Delta x}\left[\frac{u_{j+1}-u_j}{\Delta x}\left(h_{j+\frac{1}{2}}\right)^3 - \frac{u_j-u_{j-1}}{\Delta x}\left(h_{j-\frac{1}{2}}\right)^3\right]\\ &= \frac{1}{3(\Delta x)^2}\left[\frac{\left(h_{j+\frac{1}{2}}\right)^3}{\overline{h}_{j+1}}\,\overline{q}_{j+1} - \frac{\left(h_{j+\frac{1}{2}}\right)^3 + \left(h_{j-\frac{1}{2}}\right)^3}{\overline{h}_j}\,\overline{q}_j + \frac{\left(h_{j-\frac{1}{2}}\right)^3}{\overline{h}_{j-1}}\,\overline{q}_{j-1}\right], \end{aligned} \tag{2.10}$$

$$\begin{aligned} \left(\frac{1}{2}h^2B_xu\right)_x(x_j) &= \left(\frac{1}{2}hB_xq\right)_x(x_j) \approx \frac{1}{2\Delta x}\left[h_{j+\frac{1}{2}}(B_x)_{j+\frac{1}{2}}q_{j+\frac{1}{2}} - h_{j-\frac{1}{2}}(B_x)_{j-\frac{1}{2}}q_{j-\frac{1}{2}}\right]\\ &= \frac{1}{4\Delta x}\left[h_{j+\frac{1}{2}}(B_x)_{j+\frac{1}{2}}\overline{q}_{j+1} + \left(h_{j+\frac{1}{2}}(B_x)_{j+\frac{1}{2}} - h_{j-\frac{1}{2}}(B_x)_{j-\frac{1}{2}}\right)\overline{q}_j - h_{j-\frac{1}{2}}(B_x)_{j-\frac{1}{2}}\overline{q}_{j-1}\right], \end{aligned} \tag{2.11}$$

$$\begin{aligned} \left(\frac{1}{2}B_xh^2u_x\right)(x_j) &\approx \frac{1}{2}(B_x)_j\overline{h}^2_j(u_x)_j \approx \frac{1}{2}(B_x)_j\overline{h}^2_j\left[\frac{1}{\overline{h}_j}(q_x)_j - \frac{(h_x)_j}{\overline{h}^2_j}\overline{q}_j\right]\\ &= \frac{1}{4\Delta x}(B_x)_j\left[\overline{h}_j\overline{q}_{j+1} - 2\Delta x(h_x)_j\overline{q}_j - \overline{h}_j\overline{q}_{j-1}\right] \end{aligned} \tag{2.12}$$

$$(B^2_xhu)(x_j) \approx (B_x)^2_j\overline{q}_j, \tag{2.13}$$

where $u_j := \overline{q}_j/\overline{h}_j$ and

$$\begin{aligned} &u_{j+\frac{1}{2}} := \frac{1}{2}(u_{j+1}+u_j), \quad h_{j+\frac{1}{2}} := \frac{1}{2}(\overline{h}_{j+1}+\overline{h}_j), \quad q_{j+\frac{1}{2}} := \frac{1}{2}(\overline{q}_{j+1}+\overline{q}_j),\\ &(B_x)_j := \frac{B_{j+\frac{1}{2}} - B_{j-\frac{1}{2}}}{\Delta x}, \quad (B_x)_{j+\frac{1}{2}} := \frac{1}{2}((B_x)_{j+1}+(B_x)_j), \quad (q_x)_j := \frac{\overline{q}_{j+1}-\overline{q}_{j-1}}{2\Delta x}. \end{aligned} \tag{2.14}$$

We then replace the time derivatives h_t by its space equivalent $-q_x$ and use (2.14) to obtain the following discretization of N:

$$\begin{aligned} N_j = &-\frac{2}{\Delta x}\Big[h_{j+\frac{1}{2}}\cdot\frac{q_{j+1}-q_j}{\Delta x}\Big(h_{j+\frac{1}{2}}\frac{u_{j+1}-u_j}{\Delta x}-(B_x)_{j+\frac{1}{2}}u_{j+\frac{1}{2}}\Big)\\ &\qquad -h_{j-\frac{1}{2}}\cdot\frac{q_j-q_{j-1}}{\Delta x}\Big(h_{j-\frac{1}{2}}\frac{u_j-u_{j-1}}{\Delta x}-(B_x)_{j-\frac{1}{2}}u_{j-\frac{1}{2}}\Big)\Big]\\ &-2(B_x)_j(q_x)_j\Big\{(q_x)_j-[(h_x)_j+(B_x)_j]u_j\Big\}\end{aligned} \tag{2.15}$$

Remark 2.2 In equations (2.10)–(2.13), $(h_x)_j$ are obtained using the limiter as it is described in Section 2.1.1, while $(q_x)_j$ are calculated using the centered differences (see (2.14)). The latter is done to avoid the need to solve a nonlinear system of algebraic equations as we explain in Section 2.2.

Remark 2.3 We would like point out that all of the terms in (2.10)–(2.13) will be taken at either t^n or t^{n+1} depending on a particular choice of the time evolution method for the numerical integration of the system (2.2). The manner in which these terms are combined and treated is presented in Section 2.2.

2.1.3 Well-Balanced Source Discretization

Our goal is to design a numerical scheme for (1.3) that exactly preserves the "lake-at-rest" steady-state solution (1.4). This is achieved by selecting a proper discretization of the geometric source term $\overline{S}_j^{(2)}$. Such a discretization was derived for the classical Saint-Venant system in [20], and since both M_j and N_j as defined in Section 2.1.2 vanish at this steady state, we use this discretization along with an additional atmospheric pressure term for our scheme:

$$\overline{S}_j^{(2)} = -g\,\frac{\big(w^-_{j+\frac{1}{2}}-B_{j+\frac{1}{2}}\big)+\big(w^+_{j-\frac{1}{2}}-B_{j-\frac{1}{2}}\big)}{2}\cdot\frac{(B_{j+\frac{1}{2}}-B_{j-\frac{1}{2}})}{\Delta x}+p^a\,\frac{w^-_{j+\frac{1}{2}}-w^+_{j-\frac{1}{2}}}{\Delta x}.$$

2.2 Time Evolution

We solve the semi-discrete system (2.2) by applying the third-order strong stability preserving Runge-Kutta (SSP-RK) method from [15, 16], which can be written as a convex combination of three forward Euler steps. For the purpose of demonstration, we proceed by fully discretizing (2.2) according to the forward Euler method, and all results obtained from doing so also apply to the SSP-RK method used in all of our numerical experiments.

When fully discretized by the forward Euler method, the first component of (2.2) becomes

$$\overline{w}_j^{n+1} = \overline{w}_j^n - \lambda\left(H^{(1)}_{j+\frac{1}{2}} - H^{(1)}_{j-\frac{1}{2}}\right), \tag{2.16}$$

where $\lambda = \Delta t/\Delta x$. Notice that (2.16) has no contribution from $\mathcal{M}$, $\mathcal{N}$ or $\mathbf{S}$ and therefore we may advance the first component *independently* of the second one to obtain the cell averages of w at the new time level, $\{\overline{w}_j^{n+1}\}_{j=1}^N$ (and thus $\{\overline{h}_j^{n+1}\}_{j=1}^N$ since $\overline{h}_j^{n+1} := \overline{w}_j^{n+1} - B_j$, where B_j is given by (2.6)). The fully discretized version of the second component of (2.2) then becomes

$$\overline{q}_j^{n+1} + \alpha_M M_j^{n+1} = \overline{q}_j^n + \alpha_M M_j^n - \lambda\left(H^{(2)}_{j+\frac{1}{2}} - H^{(2)}_{j-\frac{1}{2}}\right) + \Delta t\overline{S}_j^{(2)} - \Delta t\alpha_N N_j^n, \tag{2.17}$$

where all of the terms on the RHS of (2.17) are taken at $t = t^n$.

Combining (2.10)–(2.13) for the discretization of M at time level t^{n+1} and inserting this into the left-hand side (LHS) of (2.17) leads to the tridiagonal system $\mathcal{T} = (\tau_{i,j}^{n+1}),\ j = 1, \ldots, N,\ i = j-1, j, j+1$ for $\{\overline{q}_j^{n+1}\}$:

$$\overline{q}_j^{n+1} + \alpha_M M_j^{n+1} = \tau_{j-1,j}^{n+1}\overline{q}_{j-1}^{n+1} + \tau_{j,j}^{n+1}\overline{q}_j^{n+1} + \tau_{j+1,j}^{n+1}\overline{q}_{j+1}^{n+1}, \tag{2.18}$$

where

$$\tau_{j-1,j}^{n+1} = \alpha_M \left[\frac{\overline{h}_j^{n+1}(B_x)_j - h_{j-\frac{1}{2}}^{n+1}(B_x)_{j-\frac{1}{2}}}{4\Delta x} - \frac{\left(h_{j-\frac{1}{2}}^{n+1}\right)^3}{3\overline{h}_{j-1}^{n+1}(\Delta x)^2}\right],$$

$$\tau_{j,j}^{n+1} = 1 + \alpha_M \left[\frac{h_{j+\frac{1}{2}}^{n+1}(B_x)_{j+\frac{1}{2}} - h_{j-\frac{1}{2}}^{n+1}(B_x)_{j-\frac{1}{2}}}{4\Delta x} + \frac{\left(h_{j+\frac{1}{2}}^{n+1}\right)^3 + \left(h_{j-\frac{1}{2}}^{n+1}\right)^3}{3\overline{h}_j^{n+1}(\Delta x)^2} + \frac{(B_x)_j(h_x)_j^{n+1}}{2} + (B_x)_j^2\right],$$

$$\tau_{j,j+1}^{n+1} = \alpha_M \left[\frac{h_{j+\frac{1}{2}}^{n+1}(B_x)_{j+hf} - \overline{h}_j^{n+1}(B_x)_j}{4\Delta x} - \frac{\left(h_{j+\frac{1}{2}}^{n+1}\right)^3}{3\overline{h}_{j+1}^{n+1}(\Delta x)^2}\right].$$

Notice that the term $\overline{q}_j^n + \alpha_M M_j^n$ on the RHS of (2.17) is discretized in the same way, but at time level $t = t^n$.

Remark 2.4 The addition of the dispersive terms M and N does not affect the well-balanced property of the scheme because these terms vanish at the "lake-at-rest" steady state (1.4). The positivity-preserving property of the scheme is also unaffected because these terms do not appear in the first equation of (1.1).

Remark 2.5 We may write the LHS of (2.17) as described by (2.18) as $\mathcal{T}\mathbf{q}^{n+1}$, where $\mathbf{q}^{n+1}$ is the vector of the unknown cell averages $\{\overline{q}_j^{n+1}\}_{j=1}^N$. When using free boundary conditions, $\mathcal{T}$ will be strictly tridiagonal, and it is well-known that in this case, the linear algebraic system (2.17) can be efficiently solved using the LU decomposition; see, e.g., [8, 34] for details. In the case of periodic boundary conditions, the matrix $\mathcal{T}$ becomes circulant and one may still take advantage of the banded structure of the matrix by implementing the Sherman-Morrison algorithm proposed in [32].

3 Numerical Experiments

In the following experiments, we will examine the role that the non-hydrostatic pressure terms play in the long-time propagation of water waves. We will use the classical Saint-Venant system for comparison, which is simply (1.3) with $\alpha_M = \alpha_N = p^a \equiv 0$. In all of the experiments, we take $p^a \equiv 0$, take the minmod parameter $\theta = 1.3$, and consider free boundary conditions.

Example 1 — Solitary Wave Propagation

In the first example (taken from [5]), we study propagation of the wave given by the following initial data:

$$h(x,0)=1+\frac{1}{10}\operatorname{sech}^2\Big(\sqrt{\frac{3}{40}}(x-70)\Big),\quad u(x,0)=\frac{\sqrt{g}}{10}\operatorname{sech}^2\Big(\sqrt{\frac{3}{40}}(x-70)\Big),$$

over a flat bottom topography with $B(x)\equiv -0.1$. We take $g=9.81$ and divide the computational domain $[0,400]$ into 3200 finite-volume cells. According to [5], in the case when $\alpha_M=\alpha_N=1$, these data correspond to a solitary wave, which is a single elevation of water surface above an undisturbed surrounding, which is neither preceded nor followed by any free surface disturbances.

In our numerical experiments below, we compute the solutions until the final time $t=50$ and demonstrate how the speed, magnitude and shape of the wave is affected by the choice of α_M and α_N. We begin with the classical Saint-Venant system ($\alpha_M=\alpha_N=0$) and then start adding the non-hydrostatic pressure terms by gradually increasing α_M and α_N. We first observe that for a very small value of $\alpha_M=\alpha_N=0.01$, the solutions of hydrostatic and non-hydrostatic systems are almost the same except for a small change of the shape of the wave at the top; see Figure 3.1. We then further increase α_M and α_N to 0.02–0.05 and observe that up to the intermediate times (around $t=20$) the solution magnitude increases before decreasing at later times. One can also observe a substantial change in the shape of the wave as a dispersive wave structure clearly develops for $\alpha_M=\alpha_N=0.04$ and 0.05; see Figure 3.2. When α_M and α_N are increased up to 0.01, the magnitude of the wave seem to increase up to about $t=30$ and then it stabilizes; for even larger values of $\alpha_M=\alpha_N=0.25$ and 0.5, the dispersive wave structure starts disappearing and the amplitude growth becomes less pronounced; and for $\alpha_M=\alpha_N=1$ the expected solitary wave structure is numerically recovered; see Figure 3.3. Finally, in Figure 3.4, we show the solution obtained for larger dispersive coefficients $\alpha_M=\alpha_N=2$ and 5. As one can see, in these two cases the magnitude of the wave decreases and a wave train is clearly formed.

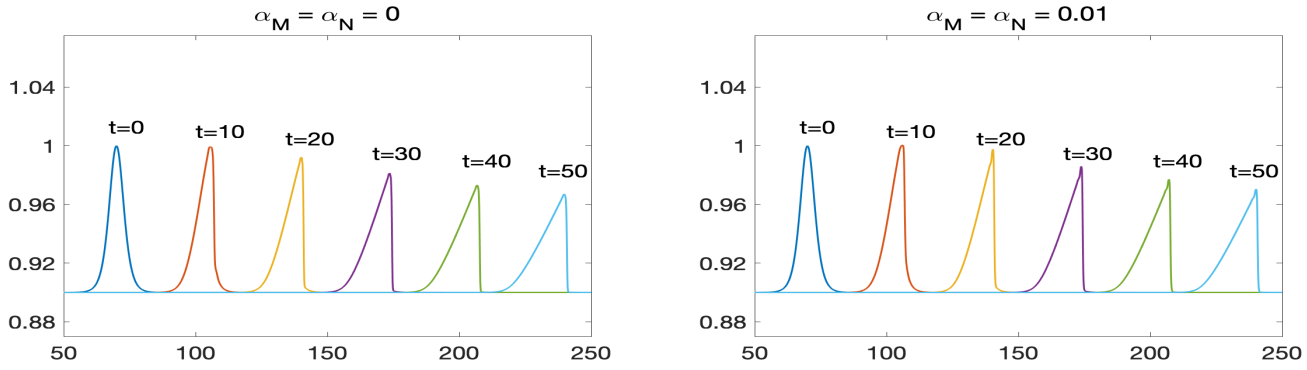

Figure 3.1: Example 1: Time evolution of the water surface for $\alpha_M=\alpha_N=0$ (left) and 0.01 (right).

We also perform an experimental convergence study of the proposed method. To this end, we take the solution computed with $\alpha_M=\alpha_N=1$ at time $t=0.1$ on different grids and compare them with the reference solution obtained with 51200 finite-volume cells. The results are reported in Tables 3.1 and 3.2 for w and q, respectively. as One can observe, the expected second order of convergence is achieved in both L^∞-, L^1- and L^2-norms.

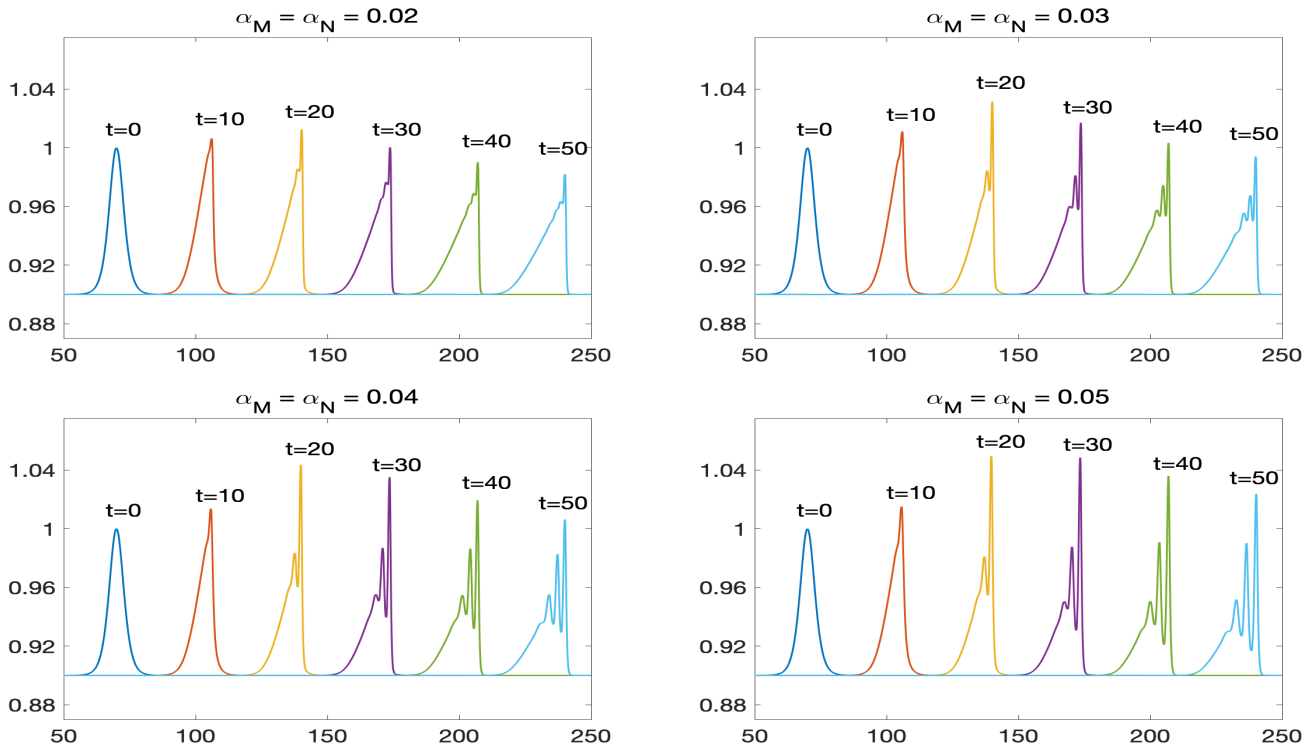

Figure 3.2: Example 1: Time evolution of the water surface for $\alpha_M = \alpha_N = 0.02$ (top left), 0.03 (top right), 0.04 (bottom left) and 0.05 (bottom right).

Example 2 — Large-Scale Tsunami-Like Wave Propagation

In the second example, we consider a wave that was created using a Savage-Hutter type model of submarine landslides and generated tsunami waves. This model is governed by a two-layer system in which the lower layer is considered to be a fluid-granular mixture that has a larger density than the upper layer, which is water. The lower layer slides down the slope of the solid bottom, and the through momentum exchange causes waves to form at the water surface. For more details of this system and associated numerical methods, see [13, 18, 22].

The initial data are obtained from [22, Section 4.5], where a submarine landslide on the ocean floor creates surface waves traveling to the left and right. We choose the right-moving wave at $t = 0.3$ as the initial condition for the non-hydrostatic system (1.3) and the following bottom topography function:

$$B(x) = \begin{cases} -5, & x < 0, \\ -5 + \sum_{i=1}^{5} C_i \sin(\pi(x - S_i)/L_i), & x \geq 0, \end{cases} \tag{3.1}$$

where the parameters C_i, S_i and L_i are given in Table 3.3. The initial water surface $w(x, 0)$ and velocity $u(x, 0)$ are plotted in Figure 3.5 and a nonflat part of the bottom topography is shown in Figure 3.6. In this example, the length scale is kilometers and the time scale is hours, so we take the corresponding gravity to be $g = 271008$ km/h^2. The computational domain, $[-150, 2200]$, is divided into 18800 finite-volume cells.

We compute the solutions until the final time $t = 2$ and as in Example 1 study the dependence of the computed solutions on the choice of the dispersion parameters α_M and α_N. We begin with

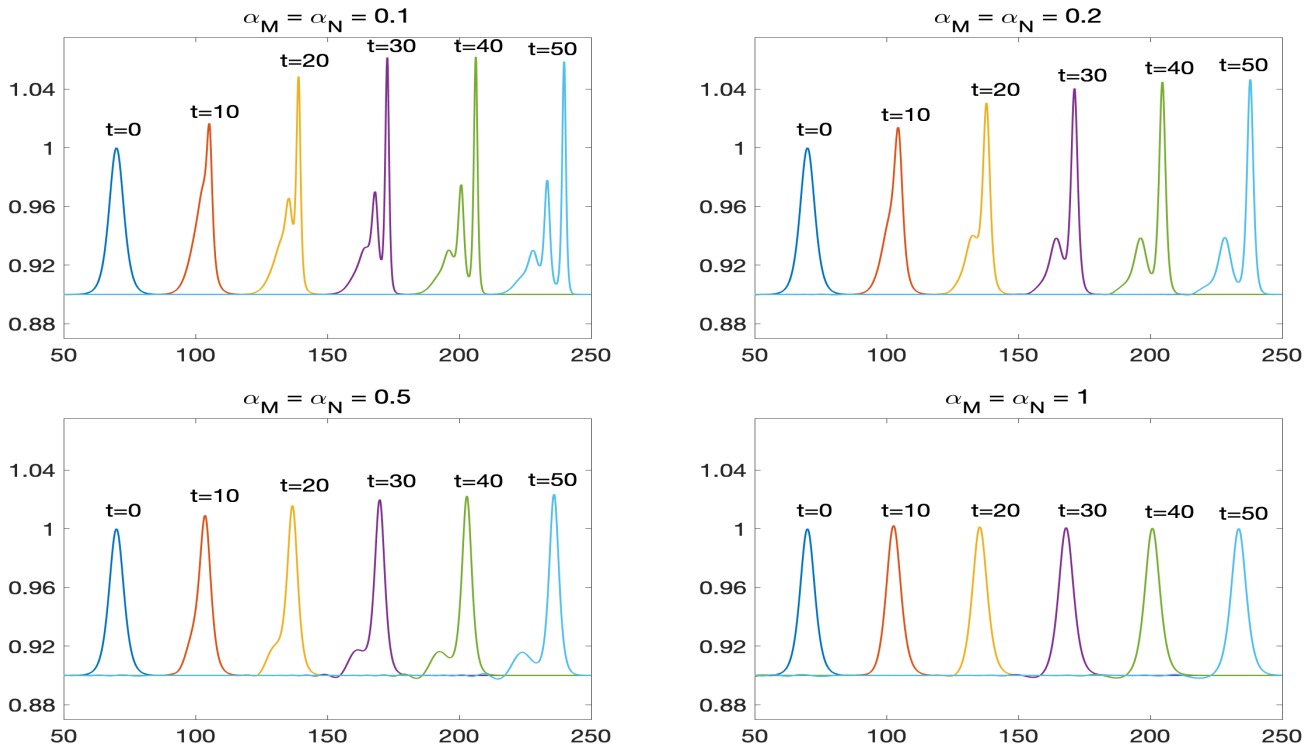

Figure 3.3: Example 1: Time evolution of the water surface for $\alpha_M = \alpha_N = 0.1$ (top left), 0.25 (top right), 0.5 (bottom left) and 1 (bottom right).

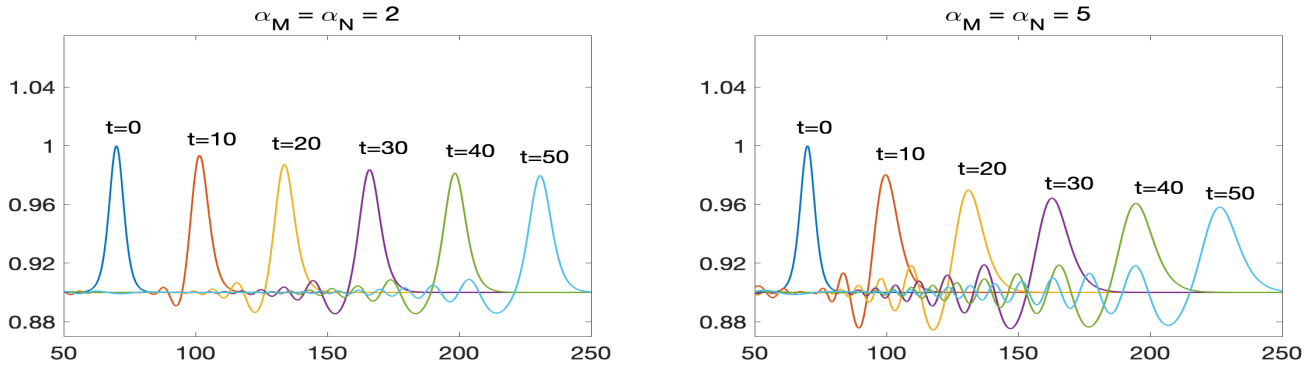

Figure 3.4: Example 1: Time evolution of the water surface for $\alpha_M = \alpha_N = 2$ (left) and 5 (right).

the classical Saint-Venant system ($\alpha_M = \alpha_N = 0$) and plot the obtained results in Figure 3.7. As one can see, there are many small waves created behind the large wave as a result of the nonflat bottom topography, but the structure of the larger waves does not seem to be significantly affected. Figure 3.8 shows time snapshots of the numerical solutions of the non-hydrostatic system (1.3) with $\alpha_M = \alpha_N = 0.05$, 0.1, 0.15 and 0.2. As expected, dispersive wave trains start appearing and become more pronounced for larger values of α_M and α_N.

Number of cells	L^∞-error	Rate	L^1-error	Rate	L^2-error	Rate
400	2.94e-04	–	1.97e-04	–	1.47e-04	–
800	9.23e-05	1.67	4.46e-05	2.14	3.54e-05	2.06
1600	1.51e-05	2.61	8.99e-06	2.31	5.53e-06	2.68
3200	2.55e-06	2.56	2.04e-06	2.14	1.01e-06	2.45
6400	6.63e-07	1.94	5.13e-07	1.99	2.31e-07	2.13
12800	1.75e-07	1.92	1.49e-07	1.79	5.88e-08	1.97

Table 3.1: L^∞-, L^1- and L^2-errors in w and the corresponding experimental rates of convergence.

Number of cells	L^∞-error	Rate	L^1-error	Rate	L^2-error	Rate
400	2.28e-04	–	4.12e-04	–	1.90e-04	–
800	5.48e-05	2.06	1.03e-04	2.00	4.62e-05	2.04
1600	1.34e-05	2.04	2.56e-05	2.01	1.12e-05	2.05
3200	2.89e-06	2.21	6.49e-06	1.98	2.78e-06	2.01
6400	7.31e-07	1.98	1.65e-06	1.98	6.94e-07	2.00
12800	1.70e-07	2.10	4.14e-07	1.99	1.71e-07	2.02

Table 3.2: L^∞-, L^1- and L^2-errors in q and the corresponding experimental rates of convergence.

i	1	2	3	4	5
C_i	0.1	0.3	0.5	0.1	1
S_i	0	2	3	0	80
L_i	40	70	100	10	2500

Table 3.3: Parameters used in for the bottom topography functions (3.1) and (3.2).

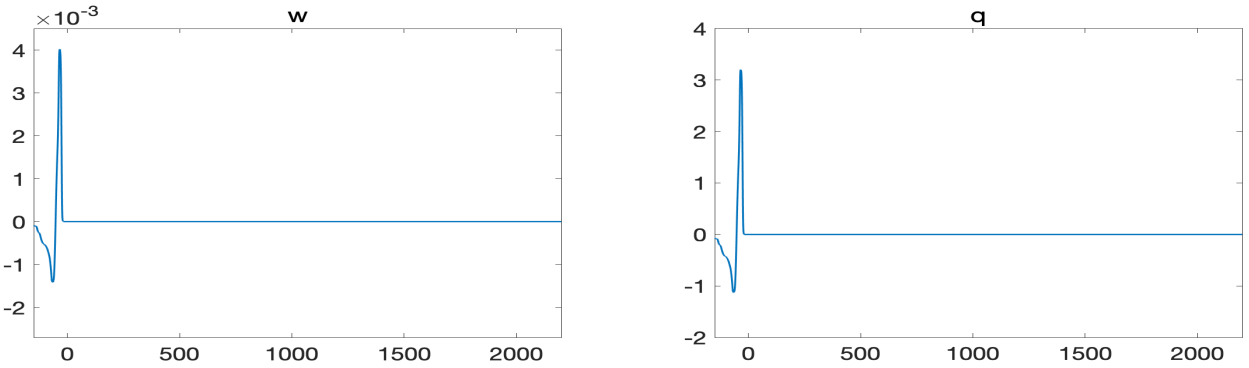

Figure 3.5: Example 2: Initial water surface (left) and discharge (right).

Example 3 — On-Shore Dynamics of the Large Wave

In order to further emphasize the difference between hydrostatic and non-hydrostatic solutions, we let the computed waves to approach the shore. We take the solutions at time $t = 2$ shown in Figure

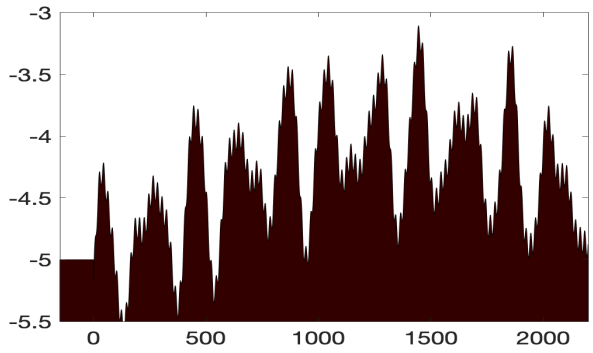

Figure 3.6: Example 2: The bottom topography function (3.1).

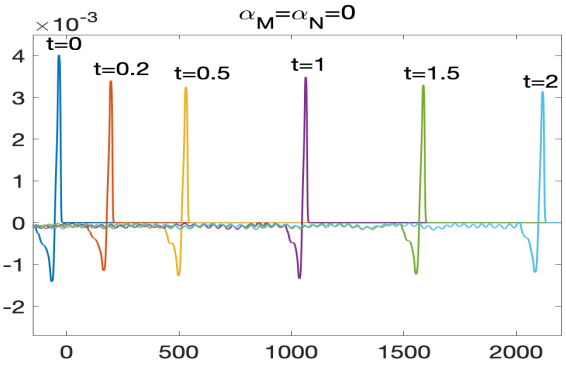

Figure 3.7: Example 2: Time evolution of the water surface for the classical Saint-Venant system ($\alpha_M = \alpha_N = 0$).

3.7 for $\alpha_M = \alpha_N = 0$ and Figure 3.8 for $\alpha_M = \alpha_N = 0.2$ as initial data in the domain $[1000, 3000]$ (divided into 16000 finite-volume cells) along with following bottom topography function:

$$B(x) = \begin{cases} -5 + \sum_{i=1}^{5} C_i \sin(\pi(x - S_i)/L_i), & x < 2200, \\ -4.86 + 2.75 \exp\left[-300\left(1 - \dfrac{x}{2600}\right)\right], & 2200 < x \le 2600, \\ 10^{-10} - 2.11 \exp\left[-300\left(\dfrac{x}{2600} - 1\right)\right], & x > 2600, \end{cases} \tag{3.2}$$

where the coefficients C_i, S_i, and L_i are given in Table 3.3. We notice that near the shore, the function B is simply a smooth curve that increases from -4.86 to almost zero; see Figure 3.9.

In order to accurately capture the on-shore arrival of the waves, we have implemented a special well-balanced reconstruction of wet/dry fronts from [2] and computed both the hydrostatic and non-hydrostatic solutions until the final time $t = 3$. We present several time snapshots of the computed water surface in Figure 3.10. As one can see, both dispersive and non-dispersive waves go through the shoaling process where they slow down and increase in height, and eventually arrive on shore. If we look closer (Figure 3.11), we see that the trailing waves actually impact how the wave comes to shore: The front of the non-hydrostatic solution is about 10–20 km behind the hydrostatic one. This suggests that the non-hydrostatic terms *must* be included in a tsunami model if one wants to accurately represent the ultimate outcome of the tsunami waves.

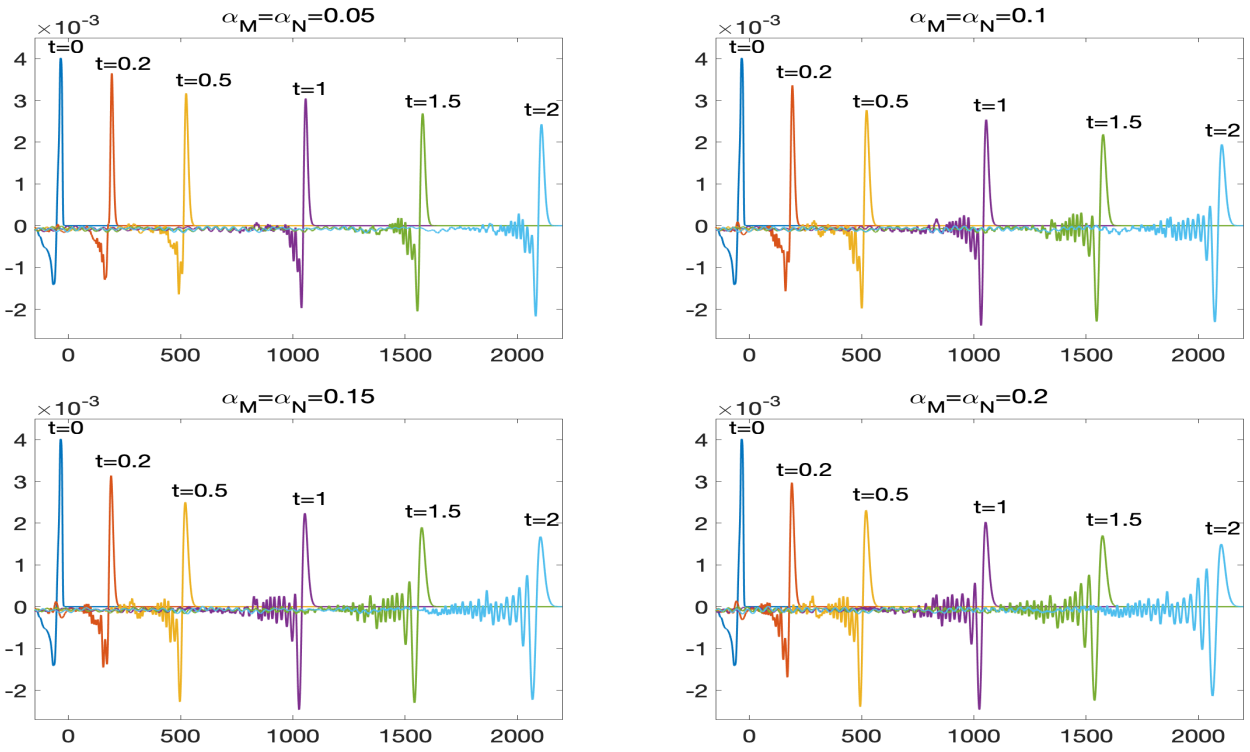

Figure 3.8: Example 2: Time evolution of the water surface for $\alpha_M = \alpha_N = 0.05$ (top left), 0.1 (top right), 0.15 (bottom left) and 0.2 (bottom right).

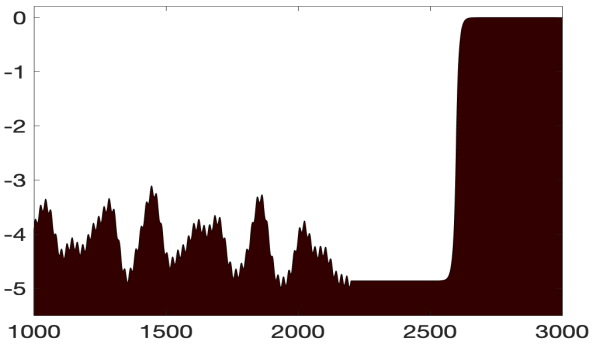

Figure 3.9: Example 3: The bottom topography function (3.2).

Acknowledgments. The work of A. Chertock was supported in part by NSF grants DMS-1521051 and DMS-1818684. The work of A. Kurganov was supported in part by NSFC grant 11771201 and NSF grants DMS-1521009 and DMS-1818666.

References

[1] E. BARTHELEMY, *Nonlinear shallow water theories for coastal waves*, Surv. Geophys., 25 (2004), pp. 315–337.

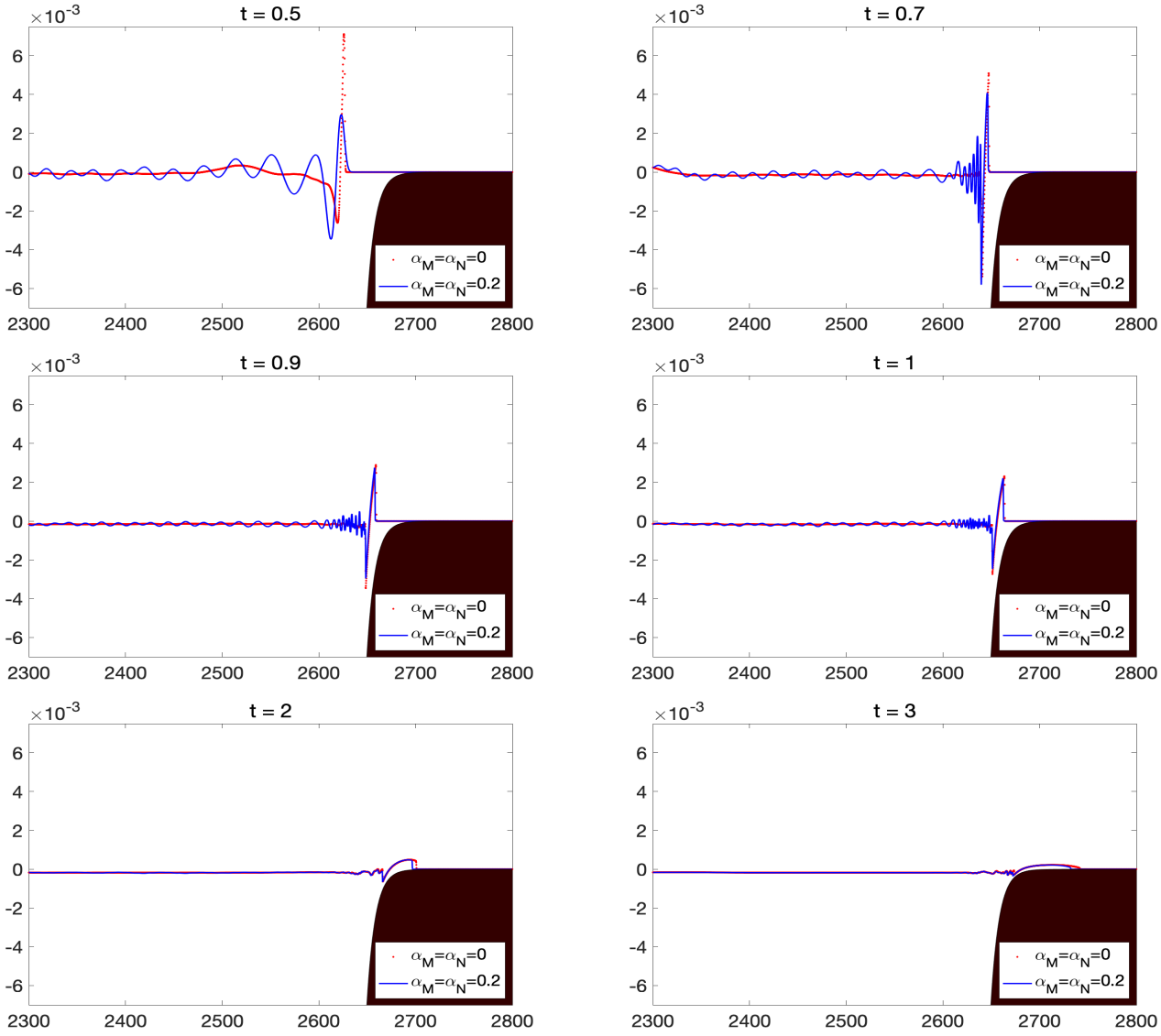

Figure 3.10: Example 3: On-shore arrival of the tsunami-like waves in the hydrostatic ($\alpha_M = \alpha_N = 0$) and non-hydrostatic with $\alpha_M = \alpha_N = 0.2$ regimes.

[2] A. BOLLERMANN, G. CHEN, A. KURGANOV, AND S. NOELLE, *A well-balanced reconstruction of wet/dry fronts for the shallow water equations*, J. Sci. Comput., 56 (2013), pp. 267–290.

[3] J. L. BONA, M. CHEN, AND J.-C. SAUT, *Boussinesq equations and other systems for small-amplitude long waves in nonlinear dispersive media. I. Derivation and linear theory*, J. Nonlinear Sci., 12 (2002), pp. 283–318.

[4] J. L. BONA, M. CHEN, AND J.-C. SAUT, *Boussinesq equations and other systems for small-amplitude long waves in nonlinear dispersive media. II. The nonlinear theory*, Nonlinearity, 17 (2004), pp. 925–952.

[5] M.-O. BRISTEAU, N. GOUTAL, AND J. SAINTE-MARIE, *Numerical simulations of a non-hydrostatic shallow water model*, Comput. & Fluids, 47 (2011), pp. 51–64.

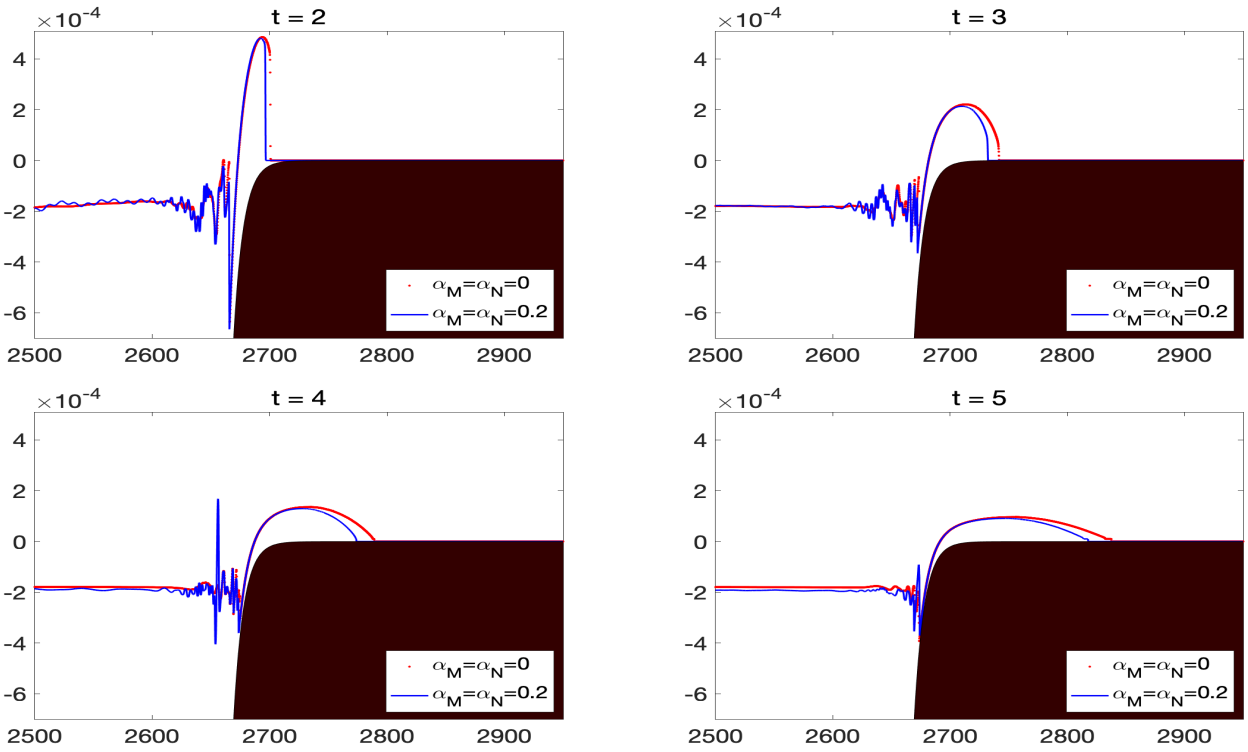

Figure 3.11: Example 3: Same as Figure 3.10, but zoomed in.

[6] M.-O. BRISTEAU AND J. SAINTE-MARIE, *Derivation of a non-hydrostatic shallow water model; comparison with Saint-Venant and Boussinesq systems*, Discrete Contin. Dyn. Syst. Ser. B, 10 (2008), pp. 733–759.

[7] E. BRYANT, *Tsunami: the Underrated Hazard*, Cambridge University Press, 2 ed., 2008.

[8] R. L. BURDEN AND D. J. FAIRES, *Numerical Analysis*, Brooks Cole, 8 ed., 2005.

[9] M. J. CASTRO DÍAZ, A. KURGANOV, AND T. MORALES DE LUNA, *Path-conservative central-upwind schemes for nonconservative hyperbolic systems*, ESAIM Math. Model. Numer. Anal. To appear.

[10] Y. CHENG AND A. KURGANOV, *Moving-water equilibria preserving central-upwind schemes for the shallow water equations*, Commun. Math. Sci., 14 (2016), pp. 1643–1663.

[11] A. CHERTOCK, S. CUI, A. KURGANOV, AND T. WU, *Well-balanced positivity preserving central-upwind scheme for the shallow water system with friction terms*, Internat. J. Numer. Meth. Fluids, 78 (2015), pp. 355–383.

[12] A. J. C. DE SAINT-VENANT, *Thèorie du mouvement non-permanent des eaux, avec application aux crues des rivière at à l'introduction des marèes dans leur lit.*, C.R. Acad. Sci. Paris, 73 (1871), pp. 147–154.

[13] E. D. FERNÁNDEZ-NIETO, F. BOUCHUT, D. BRESCH, M. J. CASTRO DÍAZ, AND A. MANGENEY, *A new Savage-Hutter type model for submarine avalanches and generated tsunami*, J. Comput. Phys., 227 (2008), pp. 7720–7754.

[14] J.-F. Gerbeau and B. Perthame, *Derivation of viscous Saint-Venant system for laminar shallow water; numerical validation*, Discrete Contin. Dyn. Syst. Ser. B, 1 (2001), pp. 89–102.

[15] S. Gottlieb, D. Ketcheson, and C.-W. Shu, *Strong stability preserving Runge-Kutta and multistep time discretizations*, World Scientific Publishing Co. Pte. Ltd., Hackensack, NJ, 2011.

[16] S. Gottlieb, C.-W. Shu, and E. Tadmor, *Strong stability-preserving high-order time discretization methods*, SIAM Rev., 43 (2001), pp. 89–112.

[17] A.E. Green and P.M. Naghdi, *A derivation of equations for wave propagation in water at variable depth*, J. Fluid Mech., 78 (1976), pp. 237–246.

[18] Ph. Heinrich, A. Piatanesi, and H. Hebert, *Numerical modelling of tsunami generation and propagation from submarine slumps: the 1998 Papua New Guinea event*, Geophys. J. Int., 145 (2001), pp. 97–111.

[19] A. Kurganov, *Finite-volume schemes for shallow-water equations*, Acta Numer., 27 (2018), pp. 289–351.

[20] A. Kurganov and D. Levy, *Central-upwind schemes for the Saint-Venant system*, M2AN Math. Model. Numer. Anal., 36 (2002), pp. 397–425.

[21] A. Kurganov and C.-T. Lin, *On the reduction of numerical dissipation in central-upwind schemes*, Commun. Comput. Phys., 2 (2007), pp. 141–163.

[22] A. Kurganov and J. Miller, *Central-upwind scheme for Savage-Hutter type model of submarine landslides and generated tsunami waves*, Comput. Methods Appl. Math., 14 (2014), pp. 177–201.

[23] A. Kurganov, S. Noelle, and G. Petrova, *Semi-discrete central-upwind scheme for hyperbolic conservation laws and Hamilton-Jacobi equations*, SIAM J. Sci. Comput., 23 (2001), pp. 707–740.

[24] A. Kurganov and G. Petrova, *A second-order well-balanced positivity preserving central-upwind scheme for the Saint-Venant system*, Commun. Math. Sci., 5 (2007), pp. 133–160.

[25] A. Kurganov and G. Petrova, *Central-upwind schemes for two-layer shallow equations*, SIAM J. Sci. Comput., 31 (2009), pp. 1742–1773.

[26] A. Kurganov and E. Tadmor, *New high resolution central schemes for nonlinear conservation laws and convection-diffusion equations*, J. Comput. Phys., 160 (2000), pp. 241–282.

[27] R. J. LeVeque, D. L. George, and M. J. Berger, *Tsunami modelling with adaptively refined finite volume methods*, Acta Numer., 20 (2011), pp. 211–289.

[28] K.-A. Lie and S. Noelle, *On the artificial compression method for second-order nonoscillatory central difference schemes for systems of conservation laws*, SIAM J. Sci. Comput., 24 (2003), pp. 1157–1174.

[29] A. Mercado-Irizarry and P. L. F. Liu, *Caribbean Tsunami Hazard*, World Scientific, 2006.

[30] H. Nessyahu and E. Tadmor, *Nonoscillatory central differencing for hyperbolic conservation laws*, J. Comput. Phys., 87 (1990), pp. 408–463.

[31] M. Ortiz, E. Gomez-Reyes, and H. Velez-Munoz, *A fast preliminary estimation model for transoceanic tsunami propagation*, Geofis. Int., 39 (2000), pp. 207–220.

[32] J. Sherman and W. J. Morrison, *Adjustment of an inverse matrix corresponding to a change in one element of a given matrix*, Ann. Math. Statistics, 21 (1950), pp. 124–127.

[33] P. K. Sweby, *High resolution schemes using flux limiters for hyperbolic conservation laws*, SIAM J. Numer. Anal., 21 (1984), pp. 995–1011.

[34] L. Trefethen and D. Bau, *Numerical Linear Algebra*, Society for Industrial and Applied Math, 1997.